Frontiers of Information Technology & Electronic Engineering
www.zju.edu.cn/jzus; engineering.cae.cn; www.springerlink.com
ISSN 2095-9184 (print); ISSN 2095-9230 (online)
E-mail: jzus@zju.edu.cn

Biologically inspired model of path integration based on head direction cells and grid cells*

Yang ZHOU‡, De-wei WU

(*College of Information and Navigation, Air Force Engineering University, Xi'an 710077, China*)

E-mail: yydayl@sina.cn; wudewei74609@126.com

Received Oct. 21, 2015; Revision accepted Mar. 16, 2015; Crosschecked Apr. 11, 2016

Abstract: Some neurons in the brain of freely moving rodents show special firing pattern. The firing of head direction cells (HDCs) and grid cells (GCs) is related to the moving direction and distance, respectively. Thus, it is considered that these cells play an important role in the rodents' path integration. To provide a bionic approach for the vehicle to achieve path integration, we present a biologically inspired model of path integration based on the firing characteristics of HDCs and GCs. The detailed implementation process of this model is discussed. Besides, the proposed model is realized by simulation, and the path integration performance is analyzed under different conditions. Simulations validate that the proposed model is effective and stable.

Key words: Head direction cells (HDCs), Grid cells (GCs), Path integration, Bionic navigation
http://dx.doi.org/10.1631/FITEE.1500364 **CLC number:** TP391; TP24

1 Introduction

Many animals can explore for food and return to their nests by using their own navigation systems. Among the various navigation systems, the path integration system plays an important role in reckoning the spatial location (Siegrist *et al.*, 2003). A path integration system can integrate the moving information, update the current location, and provide the relative relation between the current location and the reference location (Wiener *et al.*, 2010). For traditional vehicles, path integration is implemented mainly with mathematical formulas, and the ideal and simple solution is the calculus, which integrates the velocity information to obtain the displacement. For animals, path integration is achieved mainly by the internal neural mechanism in brain, such as the firing of some special cells and the information transmission among different kinds of cells (Collett and Graham, 2004; Kim and Lee, 2011; Kesner and Rolls, 2015). However, there is no accurate representation about how the brain deals with complex mathematical functions through the neural system (Kim and Lee, 2011). Therefore, for a bio-inspired vehicle whose path integration is realized based on brain science, the mathematical solution is not plausible in neurobiology. As a result, it has urged researchers in the fields of both engineering and neurobiology to develop the path integration model which is practical and biologically plausible. Finally, the fields of engineering and neurobiology can be well bridged.

With the development of biology, neuroscientists have found that there are a variety of cells in the animal brain associated with navigation. The finding includes place cells (PCs) (O'Keefe and Dostrovsky, 1971), head direction cells (HDCs) (Muir and Taube, 2004; Giocomo *et al.*, 2014), grid cells (GCs) (Hafting *et al.*, 2005; Moser and Moser, 2013), border cells (BCs) (McNaughton *et al.*, 2006), time cells (TCs) (Kraus *et al.*, 2013), and so on. These cells show special firing patterns during the moving of the

‡ Corresponding author
* Project supported by the National Natural Science Foundation of China (No. 61273048)
ORCID: Yang ZHOU, http://orcid.org/0000-0002-8384-7842

animal, and they lay a biological foundation for the study of bionic navigation of the vehicle. For path integration, it is realized by accumulating the direction and distance. If the vehicle wants to achieve path integration by a bionic approach, it should firstly have the ability to perceive the direction and distance. Among the navigation associated cells, the firing of HDCs and GCs is related to animal's moving direction and distance, respectively. Each HDC has its preferred direction. When the animal's moving direction is consistent with the preferred direction, the corresponding HDC will have a maximum firing rate (Taube, 1998). In the application, HDCs provide a strategy to encode spatial direction, and the existing model includes the self-organizing vector quantization model (Oshiro *et al.*, 2008), velocity modulated model (Erdem and Hasselmo, 2014), model based on continuous attractor neural network (Kyriacou, 2011), and so on. For the metric of distance, Hafting *et al.* (2005) found some neurons in rat entorhinal cortex. These neurons have regularly equilateral hexagon firing pattern, and thus they are called 'grid cells'. Their special firing pattern shows that GCs can be used for space transformation, and they are effective metrics for distance (Giocomo *et al.*, 2011). Currently, there is some research about path integration based on the firing characteristics of cells. Fuhs and Touretzky (2006) presented a symmetric, locally connected neural network, which can spontaneously produce a hexagonal grid of activity bumps on a two-dimensional sheet of units, and the animal's location can be obtained from the population activity of GCs with different scales and orientations. Islam and Fukuzaki (2010) proposed a computational model for path integration and navigation based on HDCs and GCs, which shows that an ensemble of HDCs can accumulate distance and reckon the direction from the starting point to the present location during exploration. Kim and Lee (2011) described a neural model of path integration involving a relatively small number of neurons and discussed how well the model operates for homing navigation. Besides, they suggested that a neural structure with only a few sensor neurons can handle successfully the path integration needed for homing navigation. Walters and Stringer (2010) presented a biologically plausible model for velocity path integration of head direction, which is composed of a linked continuous attractor network and competitive network. Hirel *et al.* (2013) presented a neural network model where the spatial and temporal components of a task are merged and learned in the hippocampus as chains of associations between sensory events, and so on. In the above mentioned studies, the biological mechanism of path integration and the information transmission process between different kinds of cells were simulated, and the outcomes showed the feasibility and availability of path integration by a bionic approach. However, through the analysis of the existing path integration models, an important question, i.e., how to establish the relationship between the firing of cells and the navigation physics parameters, is not discussed well, especially the transition mechanism from the firing of cells to the navigation physics parameters. Therefore, the aim of this study is to make up their limitations and enrich bio-inspired path integration to some extent.

This paper puts forward a new biologically inspired model of path integration based on HDCs and GCs. The model makes full use of the firing characteristics of HDCs and GCs, and the navigation physics parameters are effectively associated with the firing of cells, which can finally provide path integration information for the vehicle through a bionic approach.

2 Path integration model

HDC is a kind of neuron each having its preferred direction. When the animal's head is facing to the preferred direction, the corresponding HDC responds maximally, and the response is independent of the location, posture, and behavior of the animal. The special firing of HDCs can provide an approach to perceiving the running direction for the vehicle.

GC is a kind of neuron with regularly equilateral hexagon firing pattern. GCs are activated whenever the animal is located in any vertex of the regular hexagon. Fig. 1 shows the firing pattern of a single GC in a biological experiment (Giocomo *et al.*, 2011). The firing rate (FR) map is color encoded in Fig. 1b. Usually, the firing pattern is described by four parameters, i.e., spacing, orientation, phase, and firing field. The spacing is the distance between two

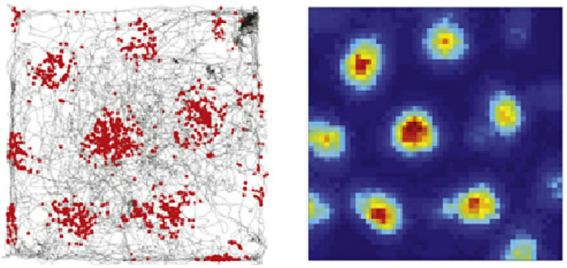

Fig. 1 Firing pattern of grid cells (GCs) recorded in a biological experiment (Giocomo *et al.*, 2011) (References to color refer to the online version of this figure)

(a) Activity trajectory and firing location (the gray line is the trajectory of the rat, and each spike is plotted in red); (b) Firing rate map (dark blue: minimum rate; dark red: maximum rate)

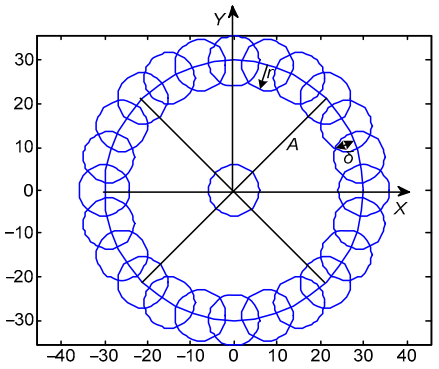

Fig. 2 Sketch map of covering the circle by the firing fields of GCs

A: grid spacing; r: firing field radius; δ: the shortest distance from the boundary of the firing field to the circle

vertices, the orientation is expressed as the angle between a camera-defined reference line (0°) and a vector to the nearest vertex of the inner hexagon in the counterclockwise direction, the phase is the spatial shift, and the firing field is the area where GCs have firing activity.

The biologically inspired model of path integration in this study makes use of the firing characteristics of HDCs and GCs. The running direction comes from the relation between HDCs and their preferred directions. Namely, different HDCs have different preferred directions, and the vehicle can perceive the running direction by comparing the FRs of all the HDCs. This process is easy to understand, and the details are not discussed here. In the following we will state mainly how to obtain the distance by the firing of GCs.

Make the starting point the center, and use a few firing fields of GCs to cover the circle that the vehicle may pass through (Fig. 2). The circle is covered by 24 firing fields of four GCs, which overlap with each other. The grid spacing is denoted by A, and the firing field radius is denoted by r. After the vehicle leaves the starting point, no matter which trajectory it chooses, at least one GC will fire when the beeline distance the vehicle has experienced is in the range of $(A-\delta, A+\delta)$ (δ is the shortest distance from the boundary of the firing field to the circle). That is to say, after the vehicle leaves the starting point, once GCs fire, the running distance can be estimated as A, and the maximum theoretical error of this estimation is r. As a result, the vehicle can obtain the running distance by the firing of GCs.

In this study, HDCs are used to measure the moving direction of the vehicle, and GCs are used to measure the moving distance of the vehicle. Besides, the distance cells (DCs) (Huhn *et al.*, 2009) are brought to associate with the HDCs to process the speed perceived by HDCs. Then DCs can indicate the relative orientation between the current location and the starting point. Finally, biologically inspired path integration can be achieved. The main process is shown in Fig. 3. The running direction is related to the firing of HDCs, the relative orientation is related to the firing of DCs, and the running distance is related to the firing of GCs. During running, a few firing fields of GCs are used to cover the circle whose center is the starting point and whose radius is A, and then the vehicle realizes path integration by the following steps:

First, HDCs perceive the speed (denoted by v_{HDC}) in their preferred direction (denoted by φ_{HDC}). On the one hand, v_{HDC} is used to calculate the FRs of HDCs, so the vehicle can know the running direction by comparing the FRs of all the HDCs. On the other hand, v_{HDC} is imported into the DCs, and the displacement (denoted by L_{DC}) along the respective preferred direction of HDCs is obtained by the processing of DCs. Second, the FRs of DCs are calculated based on L_{DC}, and the vehicle can know the relative orientation between the current location and the starting point by comparing the FRs of all the DCs. Besides, L_{DC} is imported into GCs, and the FRs of GCs (denoted by R_{GC}) are calculated by the GCs model, so the vehicle can obtain the running distance

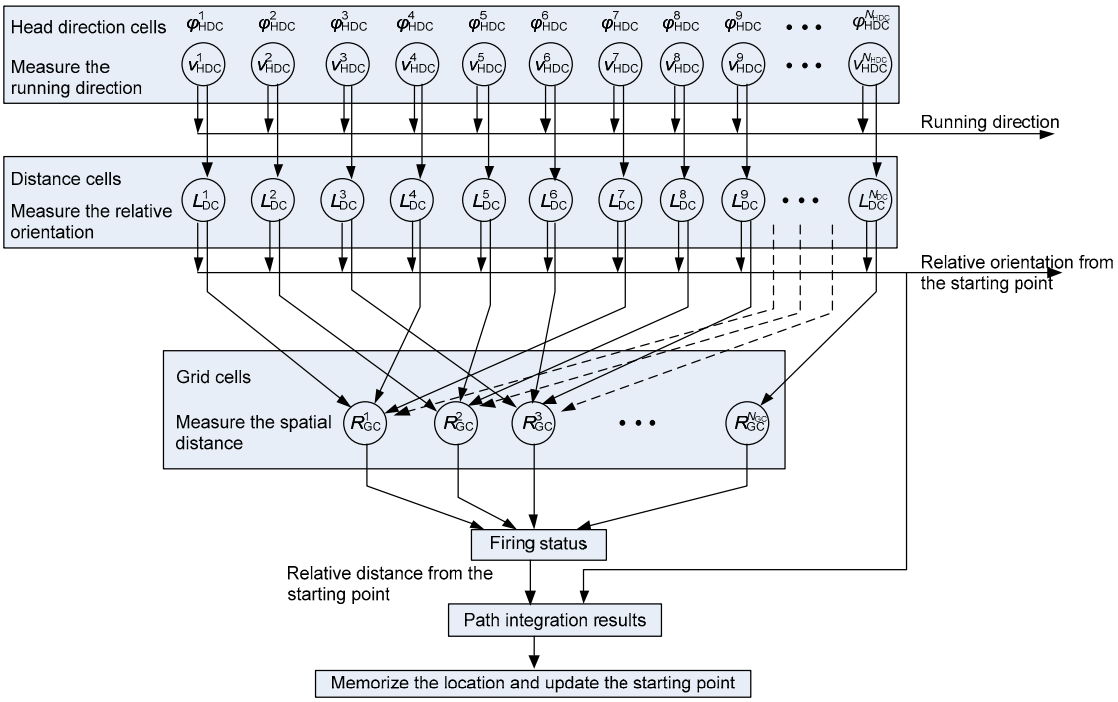

Fig. 3 Process of path integration

by detecting the firing status of GCs. Third, if GCs fire at a certain location, the vehicle thinks the beeline distance it has experienced from the starting point is *A*, and the orientation offered by DCs at the current location is its relative orientation from the starting point. Therefore, in a single cycle, the vehicle can realize path integration by combining the distance and orientation. Fourth, the location with GCs firing is memorized, and this location is regarded as the starting point for the next cycle of path integration. Finally, by repeating the above steps, the vehicle can achieve path integration during the entire running. The details of each step will be discussed in the following sections.

2.1 Head direction cells and direction

Let N_{HDC} be the total number of HDCs (for association with the GCs below, let N_{HDC} be the multiple of six). Make the direction of 0° be the reference direction, and the preferred direction of HDC i is denoted by $\varphi_{\mathrm{HDC}}^{i}$:

$$\varphi_{\mathrm{HDC}}^{i}=(i-1)\frac{360^{\circ}}{N_{\mathrm{HDC}}},\quad i=1,2,...,N_{\mathrm{HDC}}. \tag{1}$$

Let v_{HDC}^{i} be the running speed perceived by HDC i in the preferred direction. The FR of HDC i (denoted by R_{HDC}^{i}) is calculated by the following formula:

$$R_{\mathrm{HDC}}^{i}=\frac{v_{\mathrm{HDC}}^{i}-\min\limits_{j=1,2,...,N_{\mathrm{HDC}}}(v_{\mathrm{HDC}}^{j})}{\max\limits_{j=1,2,...,N_{\mathrm{HDC}}}(v_{\mathrm{HDC}}^{j})-\min\limits_{j=1,2,...,N_{\mathrm{HDC}}}(v_{\mathrm{HDC}}^{j})}. \tag{2}$$

By Eq. (2), the FRs of all the HDCs can be obtained, and the running direction of the vehicle is expressed by the HDC with the maximum FR.

Fig. 4 shows the FRs of HDCs and the running direction obtained by HDCs in a simulation. The number of HDCs is 36, and the measurement error of the speed is not considered. Simulation results show that the FRs of HDCs can be calculated by the perceived speed, and the vehicle can obtain the running direction by comparing the FRs among the whole HDCs. Besides, the error between the real and calculated directions is related to the number of HDCs and the precision of the perceived speed. Here it is not discussed in detail.

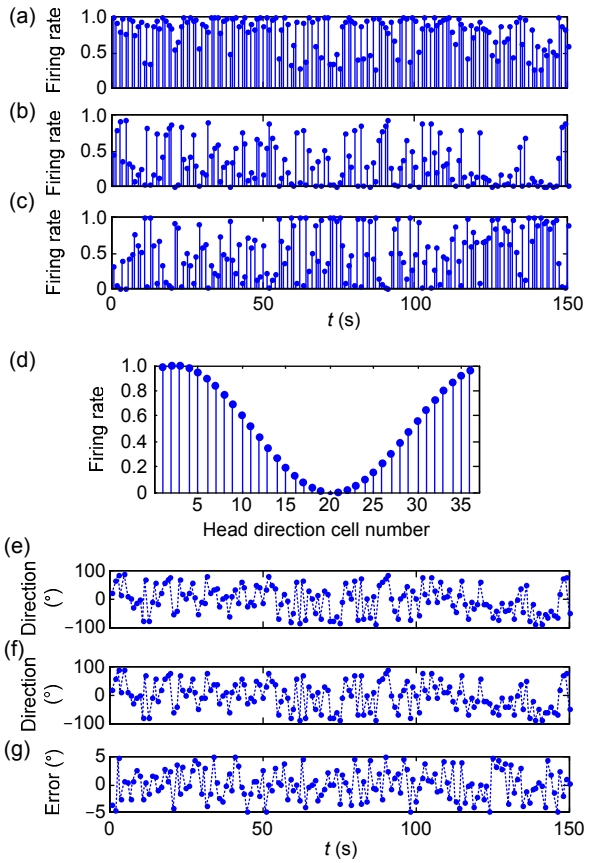

Fig. 4 Firing rates of HDCs and the calculation of the running direction: (a–c) firing rates of HDCs 4, 13, and 28 during the running, respectively; (d) firing rate of all the HDCs when the time is 4 s; (e) true running direction; (f) calculated running direction; (g) error of the calculated running direction

2.2 Distance cells and running orientation

DCs are used to deal with the speed perceived by HDCs, and they are corresponding to HDCs one by one. DCs are endowed with the concept of orientation, which is consistent with the direction of HDCs. The orientation of DCs expresses the relative relation between the vehicle's location and the starting point, but the direction of HDCs expresses the running direction of the vehicle. For example, in Fig. 5 at location ***P***, the direction expressed by HDC is φ_{HDC}, and the orientation expressed by DC is φ_{DC}.

Let $L^i_{\mathrm{DC}}(t)$ be the displacement processed by DC i. The calculation formula is as follows:

$$L^i_{\mathrm{DC}}(t)=\int_0^t v^i_{\mathrm{HDC}}(\tau)\mathrm{d}\tau,\quad i=1,2,...,N_{\mathrm{DC}},\qquad(3)$$

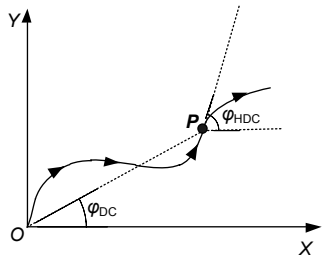

Fig. 5 Sketch map of the direction of HDC (φ_{HDC}) and the orientation of DC (φ_{DC})

where N_{DC} is the number of DCs, and N_{DC} is equal to N_{HDC}. On the one hand, $L^i_{\mathrm{DC}}(t)$ is the input of the next step. On the other hand, $L^i_{\mathrm{DC}}(t)$ is used to calculate the FR of DC (denoted by R^i_{DC}), as shown below:

$$R^i_{\mathrm{DC}}=\frac{L^i_{\mathrm{DC}}(t)-\min\limits_{j=1,2,...,N_{\mathrm{DC}}}(L^j_{\mathrm{DC}}(t))}{\max\limits_{j=1,2,...,N_{\mathrm{DC}}}(L^j_{\mathrm{DC}}(t))-\min\limits_{j=1,2,...,N_{\mathrm{DC}}}(L^j_{\mathrm{DC}}(t))}.\qquad(4)$$

As a result, at each location, the vehicle can obtain the relative orientation from the starting point by comparing the FRs among the whole DCs, and the relative orientation at the current location is expressed by the DC with the maximum FR.

2.3 Grid cells and distance

2.3.1 Firing rates of grid cells

At present, the models that can be used to calculate the FRs of GCs include mainly recurrent network models based on continuous attractor dynamics (Burak and Fiete, 2009), independent neuron models based on oscillatory interference (Burgess *et al.*, 2007), self-organization based models (Giocomo *et al.*, 2011; Mhatre *et al.*, 2012), and the models using a residue number system (Islam and Yamaguchi, 2009). Because the calculation of GCs' FRs is just a middle course, the computational models of GCs are not discussed in detail here, and we adopt the residue number model to calculate the FRs of GCs because of its superiority of convenient operation. Besides, the residue number model is adjusted slightly here. First, the base of modulus operation is changed. Second, the FR in the firing field is encoded by a Gaussian-like function. The process of calculating the FR of a single GC is as follows:

Step 1: Let N_{GC} (N_{GC}=N_{HDC}/6) be the number of GCs, A be the grid spacing, and r be the firing field

radius. Select six DCs with the difference between their adjacent angle being π/6. Let L_{DC}^{k} (k=1, 2, …, 6) be the displacement. Then L_{DC}^{k} is processed by modulus operation, and the result is denoted by $S_k(t)$:

$$S_k(t) = \mathrm{mod}(L_{\mathrm{DC}}^{k}(t), B), \tag{5}$$

where B is the base of modulus operation. For each L_{DC}^{k}, it is transformed into the range of (0, B). The relationship between A and B is as follows:

$$B = A\cos(\pi / 6). \tag{6}$$

The reason for the existence of the proportion cos(π/6) is that: A represents the distance between two vertices, but B represents the distance between the two adjacent column structures. Fig. 6 shows their relationship. The angle between A and B is π/6.

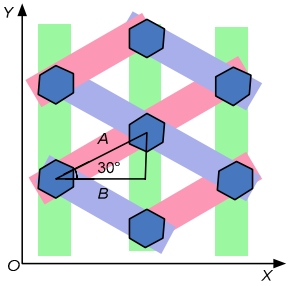

Fig. 6 Sketch map of the relationship between *A* and *B*

Step 2: Let r be the firing field radius. Then $S_k(t)$ is processed by a Gaussian-like function. The calculation formula is as follows:

$$f_k(t) = \begin{cases} \exp\left(-\dfrac{S_k^2(t)}{2\sigma_k^2}\right), & 0 \le S_k(t) \le r, \\ 0, & r < S_k(t) < B - r, \\ \exp\left(-\dfrac{(S_k(t) - B)^2}{2\sigma_k^2}\right), & \text{otherwise}, \end{cases} \tag{7}$$

where σ_k^2 is the adjustment factor of the GC firing field.

Step 3: Integrate the six $f_k(t)$. Then the FR of GC can be obtained:

$$R_{\mathrm{GC}}(t) = \prod_{k=1}^{6} f_k(t). \tag{8}$$

Through the above three steps, the FR of a single GC at a different location is obtained, and the FRs of the whole GCs can be calculated by selecting six different DCs.

Fig. 7 shows the simulation results of the firing of a single GC during the running in the space. The color represents the value of FR. The blank regions represent the locations that the vehicle has not visited. The simulation parameters include the orientations of six DCs (0°, 60°, 120°, 180°, 240°, and 300°), the running area (200×200), σ_k^2 (100), grid spacing (60), and the firing field radius (20). The simulation results show that the improved residue number model can be used to calculate the FR of a GC, and that the firing pattern is similar to that of the biological GCs. Besides, we find that the grid spacing and the firing field radius can be adjusted flexibly by changing the simulation parameters.

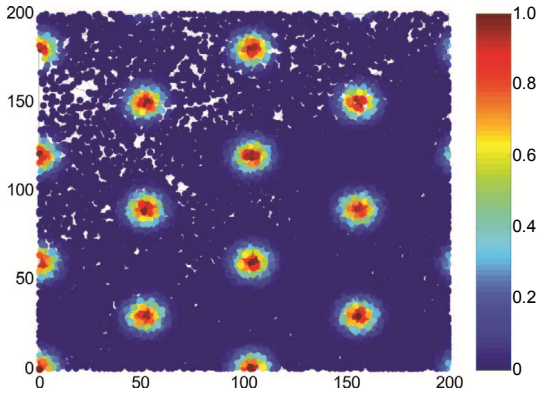

Fig. 7 Firing results of a single grid cell (GC) during the running (References to color refer to the online version of this figure)

2.3.2 Setting the grid spacing and firing field radius

The grid spacing and firing field radius influence the performance of path integration. If the setting of the grid spacing and firing field radius cannot cover the circle whose center is the starting point and the radius is grid spacing, the GCs will not fire when the vehicle passes through the blank areas. This will result in an inaccurate path integration result. If the firing field radius is large, the precision of path integration will be low. Therefore, it is very important to set the appropriate grid spacing and firing field radius.

To ensure that the firing fields of GCs can cover

the circle whose center is the starting point and whose radius is grid spacing, the grid spacing and the firing field radius should be selected suitably.

Let N_{GC} ($N_{GC}=N_{HDC}/6$) be the number of GCs, so the number of firing fields is $6N_{GC}$. When the firing fields are round and they are tangent with the adjacent firing field (Fig. 8a), the relationship between A and r is as follows:

$$r = A\sin\left(\frac{\Delta\varphi}{2}\right), \tag{9}$$

where $\Delta\varphi=2\pi/(6N_{GC})$. Therefore, to cover the circle, r should satisfy

$$r > A\sin\left(\frac{\Delta\varphi}{2}\right). \tag{10}$$

Simultaneously, to avoid the running distance between the adjacent two moments exceeding the coverage region, the shortest distance in the coverage region (denoted by d, Fig. 8b) should satisfy

$$v_{max}\Delta T < d. \tag{11}$$

Namely,

$$v_{max}\Delta T < 2\sqrt{r^2-\left(A\sin\left(\frac{\Delta\varphi}{2}\right)\right)^2}, \tag{12}$$

where v_{max} is the maximum running speed of the vehicle and ΔT is the speed updating cycle. After adjustment, r should satisfy

$$\sqrt{\frac{(v_{max}\Delta T)^2}{4}+\left(A\sin\left(\frac{\Delta\varphi}{2}\right)\right)^2} < r. \tag{13}$$

Besides, for a single GC, A and r should obey

$$\frac{r}{A} < \alpha, \tag{14}$$

where α ($0<\alpha<0.5$) is the ratio between r and A. Combining Eqs. (11), (13), and (14), the setting condition of A and r is

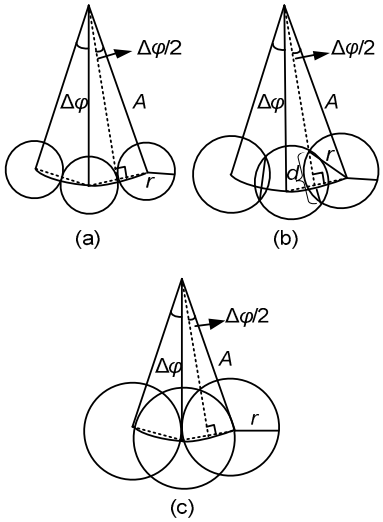

Fig. 8 Sketch map of setting the grid spacing and firing field radius: (a) firing fields are tangent; (b) firing fields are overlapping; (c) a firing field just passes through the center of the adjacent firing field

$$\begin{cases}\sqrt{\dfrac{(v_{max}\Delta T)^2}{4}+\left(A\sin\left(\dfrac{\Delta\varphi}{2}\right)\right)^2} < r < \alpha A,\\ A > \dfrac{v_{max}\Delta T}{2\sqrt{\alpha^2-\sin^2\left(\dfrac{\Delta\varphi}{2}\right)}},\\ \left|\sin\left(\dfrac{\Delta\varphi}{2}\right)\right| < \alpha < 0.5.\end{cases} \tag{15}$$

From Eq. (15), we find that r relies on A and α, and that A relies on α, so α affects directly the setting of A and r. In this study, we provide a method to set α by considering the size of the overlapping region of the adjacent firing fields.

Usually, to make the FRs of different GCs at the same location easy to distinguish, the overlapping region of the adjacent firing fields should not be too large. We assume a benchmark that a firing field just passes through the center of the adjacent firing field (Fig. 8c), so the relationship between A and r is as follows:

$$r = 2A\sin\left(\frac{\Delta\varphi}{2}\right). \tag{16}$$

As a result, α can be $2\sin(\Delta\varphi/2)$, and the setting condition of A and r is

$$\begin{cases} \sqrt{\dfrac{(v_{\max}\Delta T)^2}{4}+\left(A\sin\left(\dfrac{\Delta\varphi}{2}\right)\right)^2}<r<2A\sin\left(\dfrac{\Delta\varphi}{2}\right), \\ A>\dfrac{v_{\max}\Delta T}{\sqrt{12}\left|\sin\left(\dfrac{\Delta\varphi}{2}\right)\right|}, \\ \left|2\sin\left(\dfrac{\Delta\varphi}{2}\right)\right|<0.5. \end{cases} \tag{17}$$

Simultaneously, when A and r are adjusted appropriately, they can be selected by the following formula:

$$\begin{cases} A=\dfrac{v_{\max}\Delta T}{\sqrt{12}\left|\sin\left(\dfrac{\Delta\varphi}{2}\right)\right|}+\delta_1, \\ r=\sqrt{\dfrac{(v_{\max}\Delta T)^2}{4}+\left(A\sin\left(\dfrac{\Delta\varphi}{2}\right)\right)^2}+\delta_2, \\ \left|2\sin\left(\dfrac{\Delta\varphi}{2}\right)\right|<0.5, \\ \delta_1>0,\ \delta_2>0, \end{cases} \tag{18}$$

where δ_1 and δ_2 are the adjustment factors of A and r, respectively. Considering that r decides directly the maximum theoretical error of path integration, δ_1 and δ_2 should usually be selected as small as possible.

What is more, the shape of the firing field in this study is equilateral hexagon, which circumscribes the round (Fig. 9). So, the setting conditions provided by Eqs. (17) and (18) also satisfy the requirements of covering the circle.

Overall, when the setting of the grid spacing and firing field radius satisfies the requirements, the path integration results can be good. This will be further discussed in the simulation.

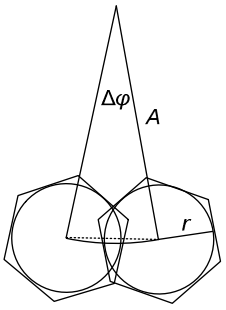

Fig. 9 Relationship between equilateral hexagon and the round

2.4 Memorizing the location and updating the starting point

Through Sections 2.1–2.3, HDCs, DCs, and GCs fire during the running of the vehicle. The vehicle can obtain the running direction by the firing of HDCs, the relative orientation from the starting points by the firing of DCs, and the relative distance from the starting point by the firing of GCs. As a result, whenever GCs fire, the vehicle thinks that the experienced relative distance from the starting point is about the distance of grid spacing, and the orientation offered by DCs at the current moment is the relative orientation from the starting point. By combining the distance and orientation, the vehicle can realize path integration in this cycle. Simultaneously, the location with GCs firing is memorized, and it is regarded as the starting point for the next cycle. Therefore, by repeating the above process, the vehicle can realize path integration during the whole running.

What is more, considering that the experienced distance may be measured multiple times in a single firing field, which will enlarge the distance measurement error, the vehicle can judge whether GCs fired a moment ago before it memorizes the location. If there was firing a moment ago, the firing of GCs at the current moment is ignored. Simultaneously, the corresponding location is not memorized, and the calculation process goes on. As a result, the vehicle can ensure the distance is measured in a single firing field no more than once.

In summary, the vehicle can achieve path integration by perceiving the firing of cells. In the next section, the realization and the performance of the model will be discussed.

3 Results and analysis

The pivot of our model is different from that of existing path integration models. In our model, the relationship between the firing of cells and the navigation physics parameters is discussed, and we focus mainly on the path integration performance that the proposed model can provide from the viewpoint of navigation. So, the analysis of the model in this study is different from that of the existing models. The simulation in this section is divided into two parts. First, path integration is carried out in beeline

running and curve running to prove that this model can be realized. Second, the influence of model parameters and the precision of perceived speed on path integration is analyzed.

3.1 Realization of the model

In the simulation, we assume that the speed perceived by HDCs is exact, and the speed remains unchanged in a speed updating cycle. The simulation parameters are listed in Table 1. Based on Eq. (18), the grid spacing A=88.28 m+δ_1, and we set A=90 m. The firing field radius r=11.60 m+δ_2, and we set r=12 m.

Table 1 Simulation parameters

Parameter	Value
Number of head direction cells (N_{HDC})	48
Number of distance cells (N_{DC})	48
Number of grid cells (N_{GC})	8
Maximum running speed (v_{max})	40 m/s
Total running time (T)	100 s
Speed updating cycle (ΔT)	0.5 s
Adjustment factor of the firing field of GC (σ^2)	50

The performance of the model is evaluated by the path integration error (PIE), and its definition is as follows:

$$\mathrm{PIE}=\sqrt{(\hat{x}-x)^2+(\hat{y}-y)^2}, \tag{19}$$

where (x, y) is the real location of the vehicle, and $(\hat{x},\hat{y})$ is the location of the vehicle estimated using the model.

3.1.1 Beeline running

In beeline running, the running direction is 22° relative to the X axis. Fig. 10 shows the FRs of some DCs during beeline running. Fig. 11 shows the FRs of GCs. Fig. 12 shows the real running trajectory and the path integration results based on the firing of the cells. Fig. 13 shows the PIE during beeline running. Obviously, the cells fire with the running of the vehicle, and the vehicle can realize path integration by perceiving the firing of the cells.

Fig. 14 shows the path integration results when the vehicle runs in different directions. In the simulation, the vehicle runs along 40 trajectories at each direction. The results in Fig. 14 are obtained by first

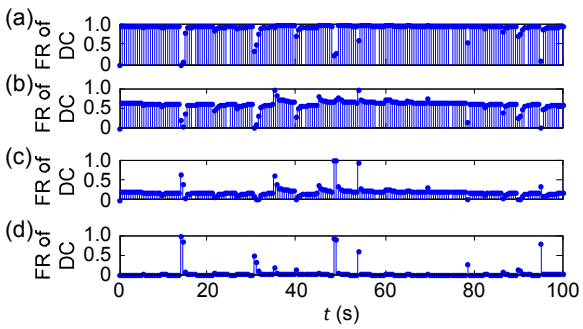

Fig. 10 Firing rates (FRs) of distance cells (DCs) 7 (a), 14 (b), 21 (c), and 28 (d) during beeline running

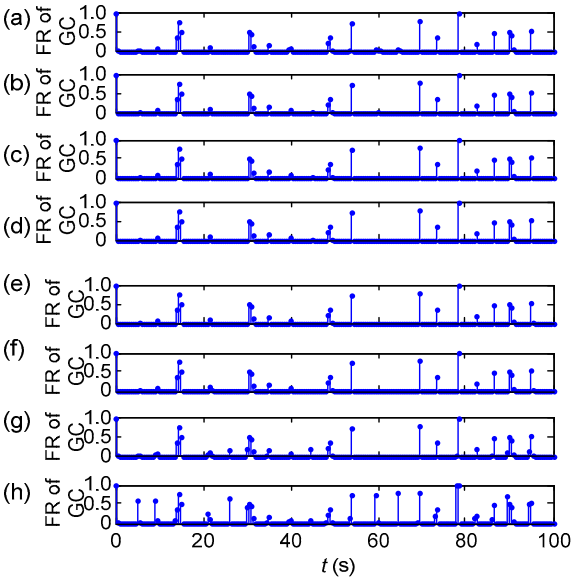

Fig. 11 Firing rates (FRs) of grid cells (GCs) 1–8 (a)–(h) during beeline running

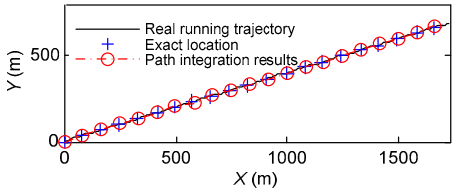

Fig. 12 Real running trajectory and path integration results for beeline running

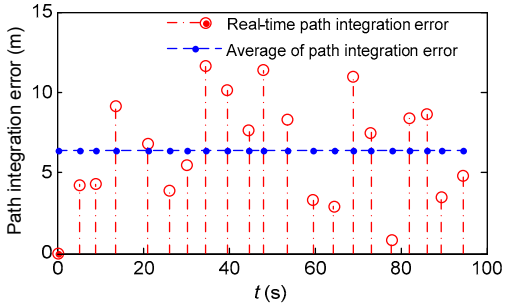

Fig. 13 Path integration error during beeline running

averaging the PIEs at all the locations for each trajectory, then averaging all the obtained average PIEs of 40 trajectories for each direction. Simulation results show that the vehicle can achieve path integration in different directions based on the firing of the cells. The average path integration error is smaller than 7.5 m, and the difference of PIE in different directions is less than 0.5 m. Thus, the simulation results also suggest that the path integration model is stable.

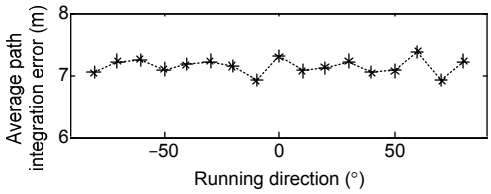

Fig. 14 Average path integration error of beeline running in different directions

3.1.2 Curve running

It has been proved that the vehicle can realize path integration for beeline running. Then how does the path integration model behave when the running direction changes with time? Fig. 15 shows the firing results of partial DCs during curve running. Fig. 16 shows the firing results of GCs. Fig. 17 shows the real running trajectory and path integration results based on the firing of the cells. Fig. 18 shows the PIE. Simulation results show that the vehicle can also realize path integration by perceiving the firing of the cells during curve running.

Fig. 19 shows the path integration results for four different curve trajectories, and the average and standard deviation of PIE are calculated. Obviously, the vehicle can realize path integration at different curving trajectories, and the difference of PIE among

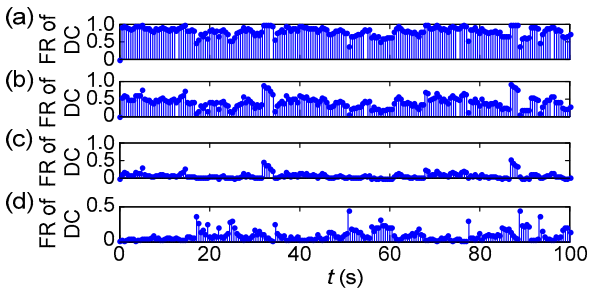

Fig. 15 Firing rate (FRs) of distance cells (DCs) 7 (a), 14 (b), 21 (c), and 28 (d) during curve running

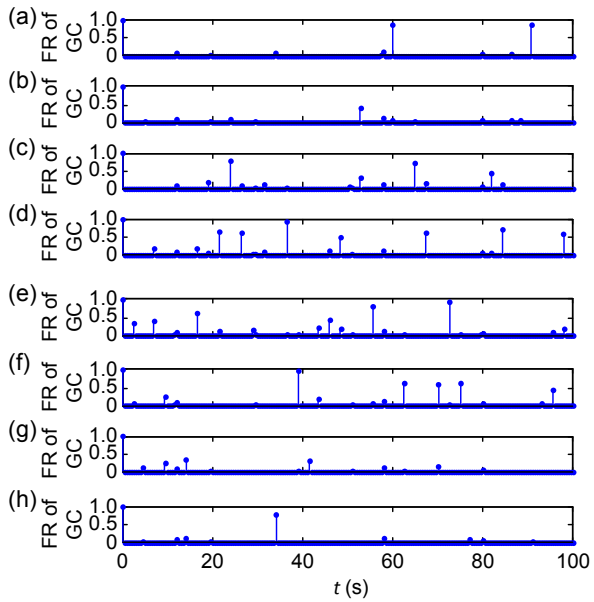

Fig. 16 Firing rate (FRs) of grid cells (GCs) 1–8 (a)–(h) during curve running

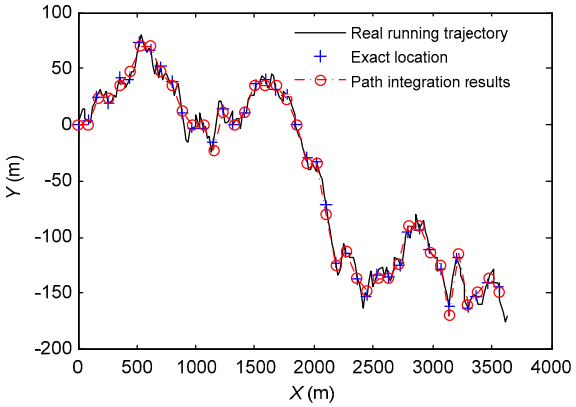

Fig. 17 Real running trajectory and path integration results during curve running

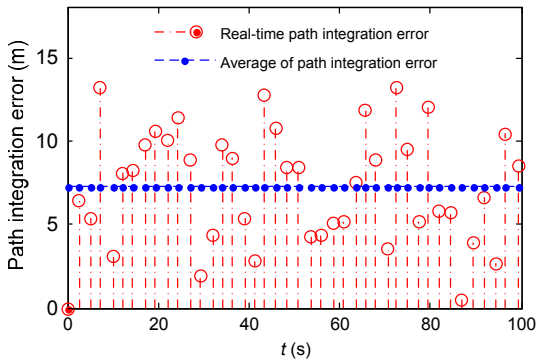

Fig. 18 Path integration error during curve running

different trajectories is small, which suggests the stability of the model.

To sum up, the path integration model based on HDCs and GCs is realizable, and the model is stable.

3.2 Influence of model parameters on path integration

The parameters related to path integration results include mainly the number of HDCs, grid spacing, and firing field radius. So, in this section we analyze mainly the influence of these three parameters on path integration. Other simulation parameters are selected according to Table 1, and the perceived speed is exact. The vehicle runs along 40 curve trajectories in the same condition. The path integration of each trajectory is evaluated by the average and standard deviation of PIE of all the locations during each trajectory, and then the path integration result in each condition is evaluated by averaging all the results obtained from the 40 trajectories.

Fig. 20 shows the path integration results with the change of the number of HDCs, grid spacing, and firing field radius. Simulation results show that these three parameters affect path integration performance. The main conclusions include: (1) For any grid spacing and any number of HDCs, PIE is large when the firing field radius is too small to cover the circle. Besides, when the firing field radius satisfies the requirement, the smaller the radius, the higher the path integration precision can be. (2) For the same grid spacing, the larger the number of HDCs, the smaller the firing field radius can be. As a result, much more HDCs can make the model reach higher precision, but path integration performance cannot be enhanced remarkably with the increase of the number of HDCs. (3) When the firing field radius satisfies Eq. (18), path integration performance is good, and the average of PIE is less than 10 m, which indicates the availability of Eq. (18).

3.3 Influence of the precision of perceived speed on path integration

For the proposed model, the input is the speed perceived by HDCs, so in this section we discuss mainly the influence of the precision of the perceived speed on path integration.

Assume that the speed error obeys Gaussian distribution with zero mean, and set the parameters

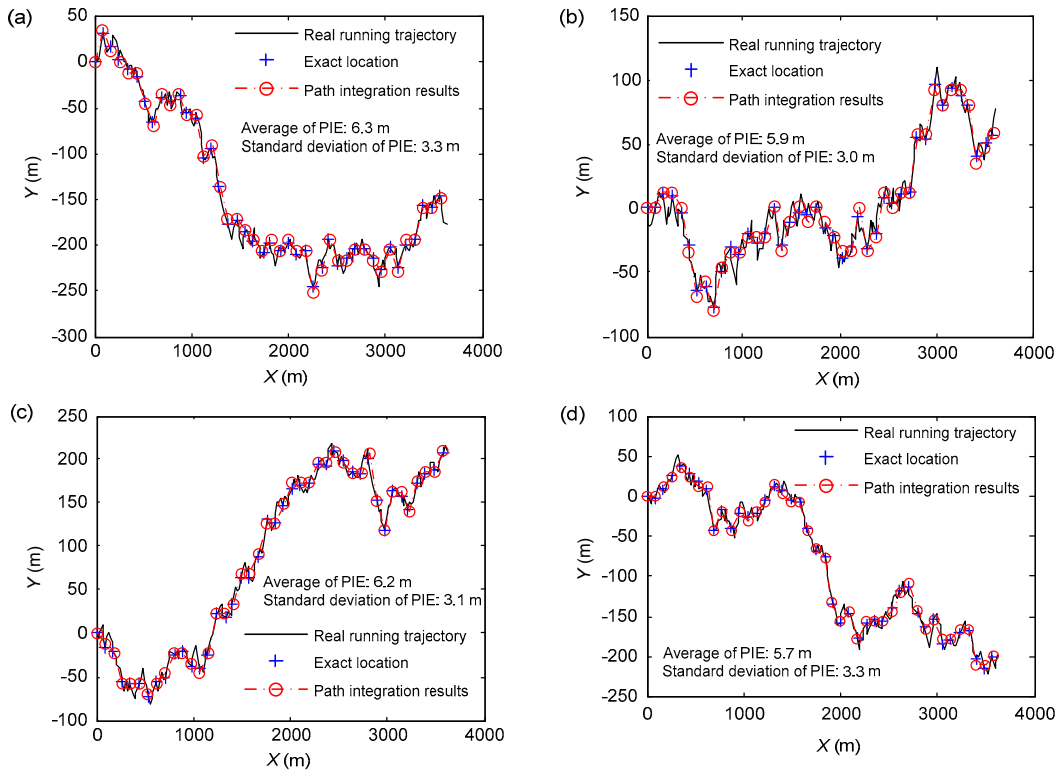

Fig. 19 Path integration results for four different curve trajectories: (a) running trajectory I; (b) running trajectory II; (c) running trajectory III; (d) running trajectory IV (PIE: path integration error)

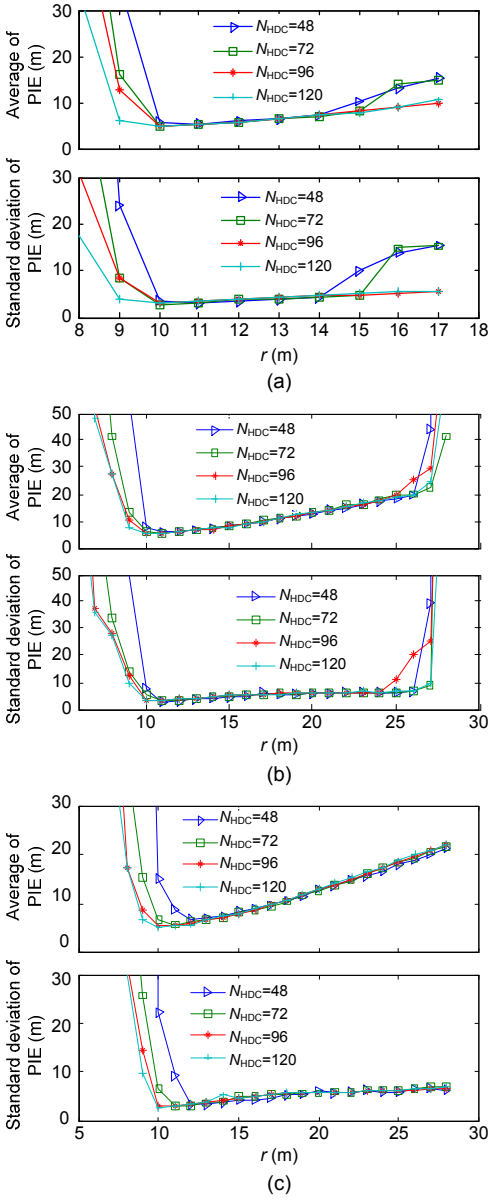

Fig. 20 Path integration error (PIE) with the change of the number of HDCs, grid spacing, and firing field radius: (a) A=60; (b) A=90; (c) A=120

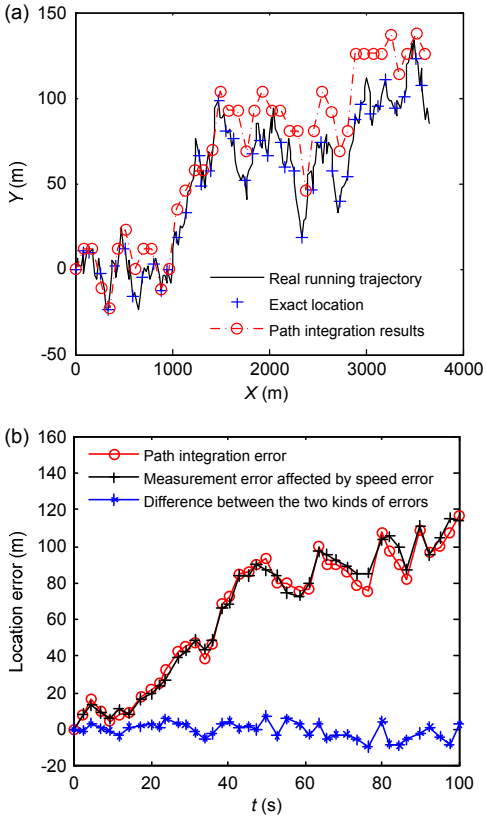

Fig. 21 Path integration results with the standard deviation of the speed error being 13.3 m/s: (a) real running trajectory and path integration results; (b) measurement error affected by the speed error and path integration error

according to Table 1. Figs. 21 and 22 show the path integration results when the standard deviation of the speed error is 13.3 m/s and 4.4 m/s, respectively. Simulation results show that the trend of the PIE is rising with time, and the accumulation error appears. This phenomenon is the same as in traditional inertial navigation systems. Usually, other external information can be used to modify the accumulation error, such as vision information. Here we do not discuss it in detail.

Fig. 23 shows the path integration results when the standard deviation of the speed error is changed. In the simulation, the vehicle runs along 40 trajectories in the same condition. The path integration result of each trajectory is evaluated by averaging the PIE at all the locations during this trajectory, and then the path integration result in each speed condition is evaluated by averaging the 40 results obtained from the 40 trajectories. Simulation results show that the changing trends of the PIE and the measurement error affected by the speed error are almost the same. That is to say, PIE caused by the model is small, and the model itself is stable. Besides, the performance of path integration is better when the speed error is smaller. For example, when the standard deviation of the perceived speed error is less than 2 m/s, the corresponding average of PIE is less than 10 m, and the standard deviation of PIE is less than 5 m.

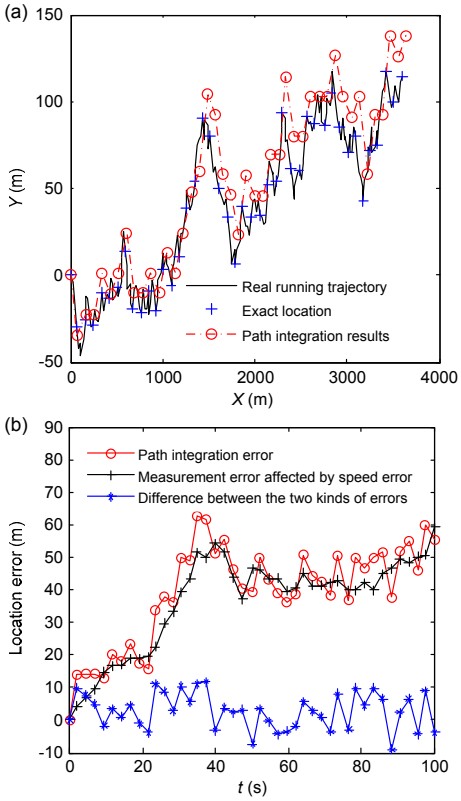

Fig. 22 Path integration results with the standard deviation of the speed error being 4.4 m/s: (a) real running trajectory and path integration results; (b) measurement error affected by the speed error and path integration error

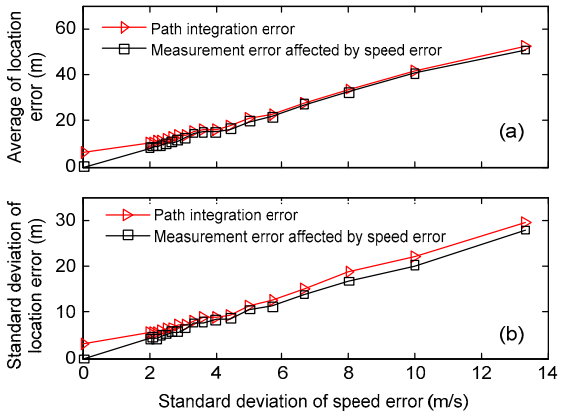

Fig. 23 Path integration results at different speed errors: (a) average location error; (b) standard deviation of the location error

4 Conclusions

Through the analysis of the research state of path integration in the fields of both engineering and neurobiology, we find that the pivots of the biological researchers (e.g., neurobiologists) and the traditional navigation researchers (e.g., roboticists and engineers) are different. The biological researchers focus mainly on using some technologies to find, prove, and simulate the biological characteristics which are associated with the navigation. Their research can open the thought and lay the biological foundation for traditional navigation researchers. However, traditional navigation researchers usually focus on explaining the navigation process from the viewpoint of physics and mathematics, and on making it into implementation by some technologies. The difference of their pivots urges the researchers to bridge the fields of engineering and neurobiology. As a result, path integration approaches will be either more practical or more biologically plausible.

In this paper, we present a biologically inspired model of path integration based on the firing characteristics of HDCs and GCs. In the model, the firing of cells is associated with the navigation physics parameters, and the path integration information is obtained based on the information transformation among different kinds of cells. Through the simulation, the path integration model proves to be realizable, and the navigation physics parameters can be obtained by perceiving the firing of HDCs and GCs, which shows the validity of the relationship between navigation physics parameters and the firing of cells. Besides, we find that the model parameters, such as the number of HDCs, grid spacing, and the firing field radius, influence the path integration performance, and that the setting conditions of grid spacing and the firing field radius provided in Section 2.3.2 are effective. What is more, through the analysis of the influence of the precision of perceived speed on path integration results, we find that the changing trends of the PIE and the measurement error affected by the speed error are almost the same, which suggests that the proposed model itself is stable. Compared to the existing models, the proposed model can not only achieve the bio-inspired path integration, but also indicate more clearly a kind of corresponding relationship between the firing of cells and the navigation physics parameters (e.g., direction and distance), and it well bridges the fields of engineering and neurobiology in terms of the realization of path integration. However, considering the research

pivot of this paper, we analyze mainly the realization of the proposed model and the influence of model parameters on path integration results, and do not analyze the different models in terms of the same measurable performance criteria. We will make a further study based on the existing results in the next research work.

References

Burak, Y., Fiete, I.R., 2009. Accurate path integration in continuous attractor network models of grid cells. *PLoS Comput. Biol.*, **5**(2):e1000291. http://dx.doi.org/10.1371/journal.pcbi.1000291

Burgess, N., Barry, C., O'Keefe, J., 2007. An oscillatory interference model of grid cell firing. *Hippocampus*, **17**(9): 801-812. http://dx.doi.org/10.1002/hipo.20327

Collett, T.S., Graham, P., 2004. Animal navigation: path integration, visual landmarks and cognitive maps. *Current Biol.*, **14**(12):R475-R477. http://dx.doi.org/10.1016/j.cub.2004.06.013

Erdem, U.M., Hasselmo, M.E., 2014. A biologically inspired hierarchical goal directed navigation model. *J. Physiol.-Paris*, **108**(1):28-37. http://dx.doi.org/10.1016/j.jphysparis.2013.07.002

Fuhs, M.C., Touretzky, D.S., 2006 . A spin glass model of path integration in rat medial entorhinal cortex. *J. Neurosci.*, **26**(16):4266-4276. http://dx.doi.org/10.1523/jneurosci.4353-05.2006

Giocomo, L.M., Moser, M.B., Moser, E.I., 2011. Computational models of grid cells. *Neuron*, **71**(4):589-603. http://dx.doi.org/10.1016/j.neuron.2011.07.023

Giocomo, L.M., Stensola, T., Bonnevie, T., *et al.*, 2014. Topography of head direction cells in medial entorhinal cortex. *Current Biol.*, **24**(3):252-262. http://dx.doi.org/10.1016/j.cub.2013.12.002

Hafting, T., Fyhn, M., Molden, S., *et al.*, 2005. Microstructure of a spatial map in the entorhinal cortex. *Nature*, **436**:801-806. http://dx.doi.org/10.1038/nature03721

Hirel, J., Gaussier, P., Quoy, M., *et al.*, 2013. The hippocampo-cortical loop: spatio-temporal learning and goal-oriented planning in navigation. *Neur. Netw.*, **43**:8-21. http://dx.doi.org/10.1016/j.neunet.2013.01.023

Huhn, Z., Somogyvári, Z., Kiss, T., *et al.*, 2009. Distance coding strategies based on the entorhinal grid cell system. *Neur. Netw.*, **22**(5-6):536-543. http://dx.doi.org/10.1016/j.neunet.2009.06.029

Islam, T., Fukuzaki, R., 2010. A model of path integration and navigation based on head direction cells in entorhinal cortex. Int. Conf. on Neural Information Processing, p.82-90. http://dx.doi.org/10.1007/978-3-642-17537-4_11

Islam, T., Yamaguchi, Y., 2009. Representation of an environmental space by grid fields: a study with a computational model of the grid cell based on a column structure. Proc. Int. Joint Conf. on Neural Networks, p.14-19. http://dx.doi.org/10.1109/ijcnn.2009.5178755

Kesner, R.P., Rolls, E.T., 2015. A computational theory of hippocampal function, and tests of the theory: new developments. *Neurosci. Biobehav. Rev.*, **48**:92-147. http://dx.doi.org/10.1016/j.neubiorev.2014.11.009

Kim, D., Lee, J., 2011. Path integration mechanism with coarse coding of neurons. *Neur. Process. Lett.*, **34**(3): 277-291. http://dx.doi.org/10.1007/s11063-011-9198-5

Kraus, B.J., Robinson, R.J.II, White, J.A., *et al.*, 2013. Hippocampal ''time cells'': time versus path integration. *Neuron*, **78**(6):1090-1101. http://dx.doi.org/10.1016/j.neuron.2013.04.015

Kyriacou, T., 2011. An implementation of a biologically inspired model of head direction cells on a robot. 12th Conf. Towards Autonomous Robotic Systems, p.66-77. http://dx.doi.org/10.1007/978-3-642-23232-9_7

McNaughton, B.L., Battaglia, F.P., Jensen, O., *et al.*, 2006. Path integration and the neural basis of the 'cognitive map'. *Nat. Rev. Neurosci.*, **7**:663-678. http://dx.doi.org/10.1038/nrn1932

Mhatre, H., Gorchetchnikov, A., Grossberg, S., 2012. Grid cell hexagonal patterns formed by fast self-organized learning within entorhinal cortex. *Hippocampus*, **22**(2): 320-334. http://dx.doi.org/10.1002/hipo.20901

Moser, E.I., Moser, M.B., 2013. Grid cells and neural coding in high-end cortices. *Neuron*, **80**(3):765-774. http://dx.doi.org/10.1016/j.neuron.2013.09.043

Muir, G.M., Taube, J.S., 2004. Head direction cell activity and behavior in a navigation task requiring a cognitive mapping strategy. *Behav. Brain Res.*, **153**(1):249-253. http://dx.doi.org/10.1016/j.bbr.2003.12.007

O'Keefe, J., Dostrovsky, J., 1971. The hippocampus as a spatial map. Preliminary evidence from unit activity in the freely-moving rat. *Brain Res.*, **34**(1):171-175. http://dx.doi.org/10.1016/0006-8993(71)90358-1

Oshiro, N., Kurata, K., Yamamoto, T., 2008. A self-organizing VQ model of head-direction cells and grid cells. *Artif. Life Robot.*, **12**:206-209. http://dx.doi.org/10.1007/s10015-007-0468-2

Siegrist, C., Etienne, A.S., Boulens, V., *et al.*, 2003. Homing by path integration in a new environment. *Animal Behav.*, **65**(1):185-194. http://dx.doi.org/10.1006/anbe.2002.2036

Taube, J.S., 1998. Head direction cells and the neurophysiological basis for a sense of direction. *Prog. Neurobiol.*, **55**(3):225-256. http://dx.doi.org/10.1016/s0301-0082(98)00004-5

Walters, D.M., Stringer, S.M., 2010. Path integration of head direction: updating a packet of neural activity at the correct speed using neuronal time constants. *Biol. Cybern.*, **103**(1):21-41. http://dx.doi.org/10.1007/s00422-009-0355-0

Wiener, J.M., Berthoz, A., Wolbers, T., 2010. Dissociable cognitive mechanisms underlying human path integration. *Exp. Brain Res.*, **208**(1):61-71. http://dx.doi.org/10.1007/s00221-010-2460-7